Soft Matter

RSC Publishing

PAPER

View Article Online
View Journal | View Issue

Topological microfluidics for flexible micro-cargo concepts†

Cite this: *Soft Matter*, 2013, **9**, 7251

Anupam Sengupta,* Christian Bahr and Stephan Herminghaus

State-of-the-art microfluidic techniques rely usually on an isotropic carrier fluid, the flow of which is modulated using morphological patterns on the microchannels, or application of external fields. In the present work, we demonstrate that replacing the isotropic fluid by an anisotropic liquid crystal introduces a flexible but versatile approach to guided transport of microscopic cargo in microfluidic devices. We show that topological line defects can be threaded at will through the microfluidic channels and used as a 'soft rail' whose position is controlled through easily accessible experimental parameters. Colloid particles and small water droplets, the 'working horses' of microfluidics, are trapped and consequently guided by the defect line through the microfluidic device. Furthermore, we demonstrate controlled threading of the defect line at a channel bifurcation. Topological microfluidics introduces a unique platform for targeted delivery of single particles, droplets, or clusters of such entities, paving the way to flexible micro-cargo concepts in microfluidic settings.

Received 7th March 2013
Accepted 20th May 2013

DOI: 10.1039/c3sm50677k

www.rsc.org/softmatter

1 Introduction

In recent years, the field of microfluidics has seen major conceptual advances, and, enabled by the progress in methodology and technology, the number of applications has grown substantially.[1–4] In particular, it has been recognized that microfluidic devices can be beneficial – or instrumental – in a much greater range of applications as one moves away from utilizing homogeneous liquids as the transport medium. The use of emulsions, where typically aqueous droplets are embedded in an immiscible carrier fluid such as oil, has become known as droplet-based microfluidics.[5] Several methods have been proposed to control the motion and position of the microfluidic cargo within the carrier fluid, *e.g.*, by means of external fields[6] and 'railed microfluidics'.[7,8] The necessity of applying external fields and patterning grooves, however, imposes important limitations in terms of design possibilities and accessible parameter ranges. For instance, the conventional railed microfluidic technique has the pathway etched on the microchannel. Since this is specific for a particular channel, it hinders the flexibility in choosing the direction post channel fabrication. In addition, requirement of a complementary pattern on the colloidal particles,[7] or low channel depths for the droplets to anchor to the rails,[8] limits the possibility of introducing a generic platform for guided transport, independent of the shape, size, or the nature of the microfluidic cargo.

In the present study, we propose and demonstrate how the application of a liquid crystal in the nematic state as the carrier fluid opens up new vistas to devise flexible micro-cargo concepts, simultaneously bypassing the stated shortcomings. While nematic liquid crystals are still highly popular in the display industry, concepts beyond-the-convention are emerging.[9–12] We have recently observed topological line defects in nematic liquid crystals—generated randomly—to be of potential interest in determining an effective pathway for the microfluidic cargo.[13,14] In the present work, we show how such line defects, known as disclination lines, can be created, positioned, and navigated in a well controlled way, and we demonstrate the use of disclination lines as 'soft rails' for the transport of microscopic cargo. As model cargo elements we used isolated colloidal particles, self-assembled chains of colloidal particles, and aqueous droplets. The ability of this topological platform to cater to a diverse set of dispersed phases—independent of the shape, size, or the nature (colloids/droplets)—demonstrates a conceptually distinct yet complementary approach to guided transport of microfluidic cargo.

2 Nematic liquid crystals

Nematic liquid crystals (NLCs) are liquids consisting of low-molecular-weight organic molecules possessing a rodlike (or disklike) shape. The rodlike molecules tend to align along a

Max Planck Institute for Dynamics and Self-Organization (MPIDS), 37077 Göttingen, Germany. E-mail: anupam.sengupta@ds.mpg.de

† Electronic supplementary information (ESI) available: Five movies M1–M5 and four figures S1–S4: (M1) laying the disclination track, (M2) trap-and-transport on soft rail, (M3) principle of the measurement of particle–disclination interaction, (M4) navigating the disclination line for guided transport at the Y-junction, (M5) *in situ* switching of the path from one arm of the Y-junction to the other. Detailed legends are given in the file supplementary.pdf which also contains Fig. S1–S4 and their captions. See DOI: 10.1039/c3sm50677k

common direction, specified by a unit vector ('director'), thereby establishing an orientational order that leads to anisotropic properties. The anisotropy becomes manifest not only in static equilibrium properties such as birefringence but also in the dynamic behaviour: The viscosity of a NLC depends on the orientation of the director relative to the directions of flow velocity and flow velocity gradient, resulting in the definition of three basic viscosity coefficients.[15] Furthermore, in a shear flow, the director experiences a viscous torque leading for most compounds to an orientation of the director approximately along the flow direction. Because of the mutual coupling between flow, orientational order, and viscosity (a detailed description is provided by the continuum theory of Ericksen and Leslie[16–18]), the flow dynamics of NLCs is fundamentally different from that of isotropic liquids. For instance, changing the orientation of the director by an electric field in an electro-optic display results in an undesired flow ('backflow') of the NLC in the display that is still subject of investigation.[19] The coupling between orientational order and flow also has a pronounced effect on the hydrodynamics of topological defects in NLCs.[20] Furthermore, the flow-director coupling has been utilized to fabricate opto-fluidic systems,[21,22] and to tune the otherwise Poiseuille-like flow profiles in microchannels.[23]

Of special interest for the present study are the topological defects that occur in the director field of NLCs. In a macroscopic sample, the orientation of the director is usually not spatially uniform but varies over distances of several micrometres. Besides such continuous variations, topological defects[24] occur at which the nematic order breaks down (*i.e.*, the orientation of the director is not defined). Defects can be either points or lines, the latter being called disclination lines. The frequent occurrence of disclination lines and their appearance, when a nematic film is observed through an optical microscope, was the origin of the name 'nematic' (from the Greek word for 'thread'). The director field around a disclination line can be described by[25]

$$\phi(x,y) = s\arctan\left(\frac{y}{x}\right) + c, \quad (1)$$

where x and y are the coordinates in a plane perpendicular to the disclination line (being located at $x = y = 0$), ϕ gives the orientation of the director in the plane, c is a constant, and the parameter $s = \pm 1/2, \pm 1, \pm 3/2, \ldots$ is called the strength of the disclination line. Experimentally, only disclinations with $s = \pm 1/2$ or ± 1 are observed. Fig. 1 shows the director field around disclination lines with strength $\pm 1/2$ and $c = 0$. In the following, we show how disclination lines in microchannels can be generated on purpose and used for the transport of colloidal entities through the channels.

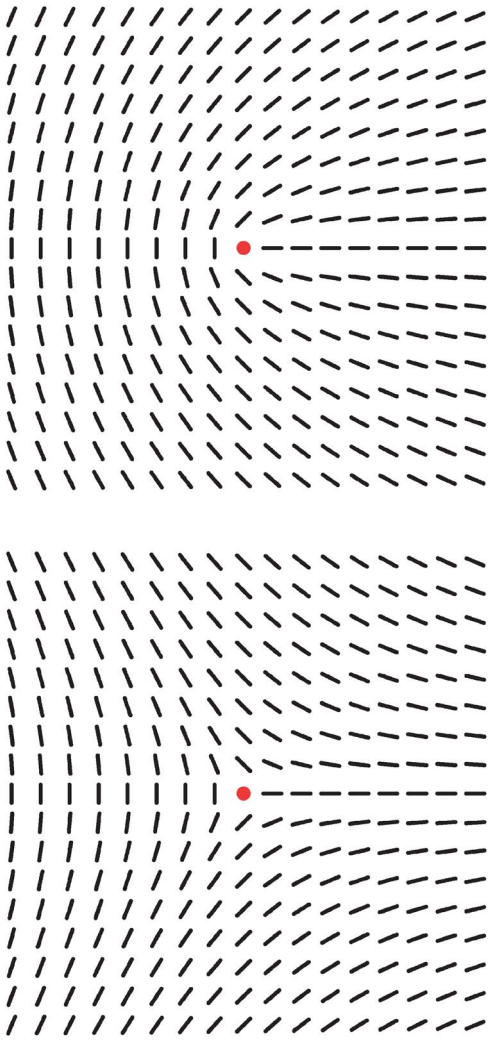

Fig. 1 Director field around a disclination line with strength $s = +1/2$ (top) and $s = -1/2$ (bottom). The dots in the centres indicate the position of the disclination lines (which run perpendicular to the plane of the images).

3 Experimental section

3.1 Preparation of the microchannels

We used linear microchannels with a rectangular cross-section which were prepared by bonding PDMS reliefs to a plane glass substrate (Fig. 2A). While the length ($l \approx 20$ mm) and the depth ($d \approx 25$ μm) of the channels were maintained unaltered throughout the experiments, the channel width (w) was varied between 50 and 500 μm. The structural stability of the microchannels with a high aspect ratio (w/d) was ensured by introducing multiple micro-pillars on the relief, in the vicinity of the inlet and the outlet ports constituting the dead volume. The surface-induced orientation of the LC molecules was perpendicular to the PDMS surface and parallel to the glass surface. On the glass surface, the orientation of the LC molecules was orthogonal to both the velocity and its gradient along the channel depth (Fig. 2B). To induce the uniform anchoring of the LC parallel to the glass surface, the glass surface was coated, prior to bonding, with a PVA solution (molecular weight 90 000, concentration 0.1% by weight) and thermally cured at 80 °C for 10 min and 110 °C for 60 min. The coated glass was then rubbed unidirectionally using a soft velvet textile. The PDMS relief was surface-bonded to the modified glass surface. This was done by briefly exposing the PDMS relief to air plasma (30 s) and pressing it mechanically on the rubbed glass, keeping the channel orthogonal to the rubbing direction. The fabricated

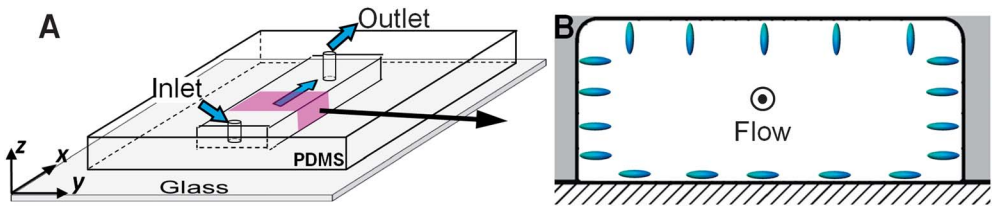

Fig. 2 Microfluidic confinement. (A) Schematic of the PDMS-glass microfluidic device. *x*, *y* and *z* indicate directions along the flow, channel width and depth, respectively. The channels were typically ≈20 mm long, ≈25 μm deep and 50–500 μm wide. (B) Channel cross-section showing the LC anchoring on the walls: glass (bottom) supports planar anchoring orthogonal to the flow velocity and its gradient. On PDMS walls, the molecules orient perpendicular to the surface. Flow is perpendicular to the image plane.

channel was left overnight before conducting experiments. This allowed the channel walls constituted by PDMS to fully recover its native surface properties, thus providing molecular alignment perpendicular to the PDMS surface.[26] To alter the angle between the flow and the initial director field, the PDMS relief was surface-bonded such that the channel made a specific, non-90-degree angle with the rubbing direction on the glass surface.[27]

3.2 Liquid crystal compound and flow control

The LC compound used in our experiments was pentylcyanobiphenyl (5CB, Synthon Chemicals), a room-temperature NLC that undergoes a transition to the isotropic phase at ≈33 °C. To operate and control the flow of 5CB through the microchannel, a gas-tight microliter syringe was filled with the NLC. The syringe was driven by a gear pump (neMESYS, Cetoni) which allowed a control of the volumetric flow rate with a precision of 1 nl h^{-1}.

3.3 Preparation of the dispersions

For the demonstration of guided transport, we used dispersions of silica microspheres (Microparticles GmbH; mean diameter 4.59 ± 0.15 μm) or aqueous droplets (polydisperse) in 5CB. The dispersed entities were first functionalized, by chemical surface functionalization in the case of the colloids and by adding suitable surfactants in the case of the aqueous droplets, to ensure a perpendicular surface anchoring. The functionalization of the silica particles was done by coating them with a monolayer of DMOAP (*N*,*N*-dimethyl-*N*-octadecyl-3-aminopropyltrimethoxysilyl chloride) which results in a strong perpendicular anchoring of the 5CB molecules.[28] The particles were immersed in a 0.1 weight% solution of aqueous DMOAP for ≈10 min, washed thoroughly with Millipore water and dried at 110 °C for 2 h. The functionalized particles were then dispersed in the isotropic phase of 5CB to produce the nematic dispersion upon cooling down. The particle concentration ranged from between 0.1% and 2%. Depending on the particle size relative to the confinement, the resulting dispersion yielded colloids with two different kinds of defect structures: Saturn-ring loop and dipolar defects.[29] For stabilizing the aqueous droplets, the cationic surfactant CTAB (Sigma Aldrich) was dissolved in de-ionized water at a concentration of ≈0.05 mM and mixed with nematic 5CB (ratio of CTAB-water to 5CB: 1 : 10 by volume). The mixture was then sonicated at room temperature for 10 min. The polydispersed droplets then showed a perpendicular anchoring at the water–5CB interface.[30] Similar to the colloidal particles, two different kinds of defect structures were observed around the droplets. Isolated droplets eventually self-assembled to form droplet chains.[31]

4 Results and discussion

4.1 Topological constraints: controlled generation of the 'soft rail'

Topological microfluidics relies on the key step of incorporating suitable topological constraints within the microchannels. While for static cases the surface anchoring of the LC molecules is decisive, additional topological constraints—due to the flow-director coupling—are induced in the presence of a flow field.[32] In the present work, our microchannels possess a rectangular cross-section with one glass and three polydimethylsiloxane (PDMS) walls (see Fig. 2A). The wall surfaces were designed to possess different anchoring conditions: the nematic director oriented itself perpendicular to the PDMS walls and parallel to the glass wall, yielding a hybrid anchoring state (Fig. 2B). The composite anchoring conditions give rise to suitable topological constraints resulting in the appearance of a disclination line in the LC-filled microchannel. In practice, the disclination line was created either by filling the channel with LC in the isotropic phase, and subsequent cooling to the nematic phase, or by filling the channel directly with the NLC.

In the first case, the channel was initially filled at a temperature at which the LC is in the isotropic phase, such as to avoid any influence of flow on the surface-induced LC anchoring. At room temperature, the LC equilibrated to the nematic phase, and the director field develops following the interplay of surface anchoring and long-range ordering, as depicted in Fig. 3A and B. At corners formed by the two PDMS walls, the alignment encounters a situation of nonconformity, which is resolved through two possible elastic deformations of the director field. In topological terms, the deformations correspond to regions of topological rank ±1/4 at each corner. The net topological charge is nevertheless conserved through the development of a singular line defect, a disclination line, of opposite strength and rank ∓1/2 within the nematic bulk. The reduced nematic order within the disclination core of radius r_c ≈ 10 nm and the associated light scattering make the defect line visible under a microscope.

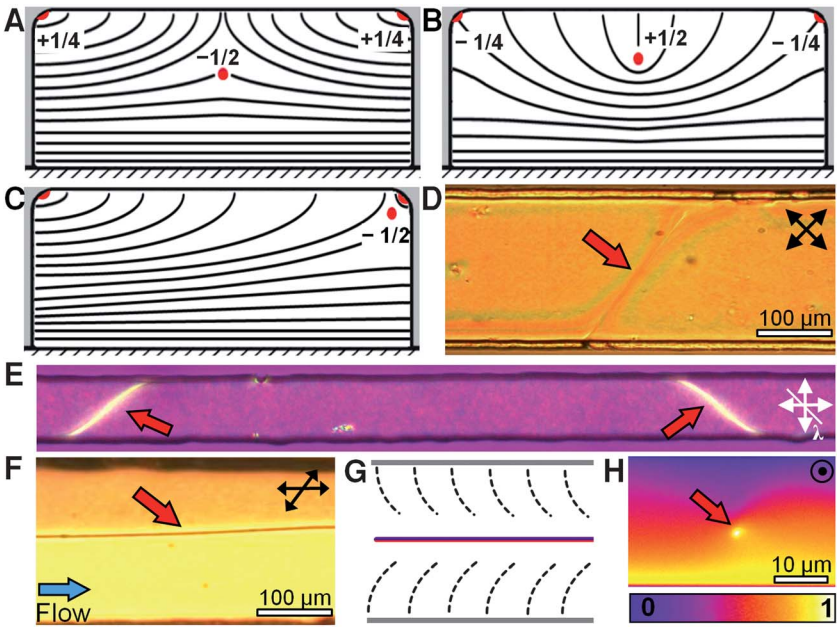

Fig. 3 Topological constraint of the director orientation leading to two possible defect structures within the hybrid channel filled with NLC 5CB. The fraction numbers refer to the strength of the topological defects. (A) Cross-sectional projection of −1/2 defect within the nematic bulk accompanied by two +1/4 defects located symmetrically at the channel corners and (B) topological complement of (A). In both the cases, the net topological charge is conserved, leaving a singular defect extending as a disclination line along the channel length. The configurations are observed in the presence of the flow or close to the isotropic–nematic transition. (C) Equilibrium director configuration corresponding to (A) in the absence of any flow. The −1/2 disclination line, placed symmetrically relative to +1/4 defects at the corners, minimizes the free energy by settling at either of the corners. (D) Consequent cross-over of the line from one to the other side of the channel (red arrow, polarized micrograph, top view). (E) Multiple cross-over along the channel length (polarized micrograph with λ-plate, top view). (F) In the presence of the flow, the disclination line is stabilized within the nematic matrix, shown here using polarized optical imaging (top view). Note that the polarizer is slightly offset from the crossed position. (G) Differential extinction of transmitted light indicates complementary director orientation on both sides of the disclination, shown by the broken lines (top view). (H) Confocal micrograph of the disclination cross-section. The imaging laser is polarized normal to the micrograph. The topological transition between the static (D) and the flow (F) states is reversible.

However, the appearance of the disclination in the vicinity of the oppositely charged defects at the channel corners yields an energetically unstable state (Fig. 3A and B). Consequently, the nematic director equilibrates to a lower energy configuration, wherein the disclination approaches the opposite topological charges obeying a (logarithmic) attractive potential.[33] In the absence of any flow, the defect line thus collapses towards one of the channel walls (see ESI Fig. S1†). The stable director configuration in equilibrium has been schematically represented in Fig. 3C (corresponding to Fig. 3A). We estimate that the bulk disclination is attracted towards a wall with a force of $F_{\text{elastic}} \approx 4\ \mu\text{N m}^{-1}$ at a separation of 1 μm away from the wall, assuming isotropic elasticity for 5CB, $K = 5.5 \times 10^{-12}$ pN. The value was arrived at using the relationships of Dafermos[34] and Ericksen.[35] It is worthwhile to note that during the isotropic-to-nematic transition, the defect equilibrates with similar probability at either wall. The equi-probability results in a cross-over of the disclination from one to the other side of the longitudinal confinement ($l \gg w$), as observed clearly in polarization micrographs (see Fig. 3D and E) of the confined NLC sample in a static case.

The stabilization of the disclination within the nematic bulk requires contributions, *e.g.* from external fields,[36] competing against the attractive interactions of elastic origin. In the present experiments, the tendency of the defects to dwell near the walls is overcome by employing viscous drag forces resulting from the flow of the LC through the channel. With the defect line initially located close to the wall, a gradual increment of the flow—at a local flow velocity of $v = 8 \pm 2\ \mu\text{m s}^{-1}$—results in the detachment of the disclination from the wall. Once detached, the disclination line is stabilized within the flowing bulk (see ESI Fig. S2†) following the interplay of the elastic and viscous forces. The elastic force F_{elastic} was effectively outweighed by a force F_{viscous} exerted on the line by the flowing medium. The threshold viscous strength was estimated to be $F_{\text{viscous}} \approx 4\ \mu\text{N m}^{-1}$, derived from the relationships reported by Ryskin and Kremenetsky[37] and Imura and Okano,[38] assuming a rotational viscosity $\gamma_1 = 0.08$ Pa s. Taking into account the uncertainties in viscosity and elastic constants, as well as the fact that the flow-director coupling was neglected, it is reasonable to conclude that F_{viscous} is strong enough to shift the static equilibrium position of the disclination line. With increasing flow speed, the disclination line was further shifted away from the wall and was finally positioned close to the mid-plane (Fig. 3F and H) at $v \approx 18\ \mu\text{m s}^{-1}$. The disclination line then stretched along the entire length of the channel and was found to be stable for flow velocities up to $v \approx 200\ \mu\text{m s}^{-1}$. Correspondingly, the director field in space comprises bend and splay elastic distortions, and can be represented as a superposition of the *xy* (Fig. 3G) and *yz* (Fig. 3A) plane projections. At even higher flow speeds,

numerous defects were generated, leading to a defect-mediated chaotic motion.[14]

Alternatively, in the second case, the disclination line was generated by simply filling the channel with 5CB in the nematic phase (see ESI Movie M1†). The molecular anchoring on the channel walls and at the air–LC interface results in the generation of a favourable topological constraint for the evolution of a $\pm 1/2$ disclination line along the channel filled with 5CB (Fig. 4A). In the nematic phase, the LC molecules anchor perpendicularly at the interface of air and 5CB.[39] However, the glass surface induced uniform planar anchoring of the NLC molecules orthogonal to the flow direction. Coexistence of the two different anchoring properties at the glass–LC–air interfaces leads to conflicting boundary conditions, which are nevertheless accommodated through a common director configuration in which the disclination line is bend towards the glass surface. This scenario was verified by focusing the microscope objective near the glass surface at high magnifications (Fig. 4B). As the meniscus proceeds downstream, the length of the defect line progressively increases, ultimately pinning itself at the outlet port of the channel. Consequently, the interplay of the topological constraints and the flow properties of NLCs can be utilized for controlled generation of long disclination lines (determined by the channel length) with a high degree of precision.

4.2 Trap-and-transport of the microfluidic cargo

The disclination line created within the channel was utilized as a 'soft rail' to transport the microscopic cargo dispersed in the nematic 5CB carrier. Our model cargo was functionalized silica colloids, 2.3 μm and 5 μm in diameter ($2a$), possessing perpendicular anchoring conditions at their surface. Due to the small size of the particles relative to the channel depth ($d \approx 25$ μm), the particles were preferentially accompanied by a dipolar defect, rather than a quadrupolar Saturn-ring defect.[29] Multiple colloids in close proximity readily formed self-assembled chains. The present system however offers a generic platform, capable of transporting both isolated particles as well as the colloidal chains. Freshly sonicated LC dispersions of colloidal particles with concentration <0.1 weight% were found to be suitable for studying the transport of isolated particles. In the vicinity of a defect line, the colloids were captured by the line (see ESI Movie M2†). Following elasticity-mediated trapping, the surrounding flow field moved the particles with the local flow velocity along the disclination track. The absolute number of dispersed entities that docked to the soft rail was increased by introducing a converging segment along the channel.

Fig. 5A shows the time sequence of the docking process of a 5 μm colloid with a Saturn-ring loop on the soft rail. The attractive potential responsible for the capture of colloids results from free-energy minimization in the disclination-particle system. Merging of the disclination and the Saturn-ring loop reduced the combined defect length by around half the loop length ($\approx \pi a$). The corresponding order of magnitude of the interaction energy can be roughly estimated as $\pi aK \approx 10^4\ kT$, with K being the isotropic elastic constant. The high order of magnitude of the interaction energy, directly dependent on the particle radius, indicates the thermodynamic robustness of the trapping phenomenon. Consequently, larger the particle radius, higher is the attractive interaction due to the disclination line.

The trapping of dipolar colloids by the defect line, shown using a micrograph sequence in Fig. 5B, is the more frequently encountered case. Unlike interactions of quadrupolar colloids, the free energy reduction owes to the evolution of a mutually conforming director configuration that minimizes the overall elastic deformation of the dipolar-disclination system. Dipolar particles are expected to exhibit attractive interactions at large, and repulsive at small separations from the disclination.[40] Qualitatively speaking, the dipolar particles simply sit on the disclination line, at an equilibrium distance from the latter, and get transported due to the local streamlines. Similarly, chains of

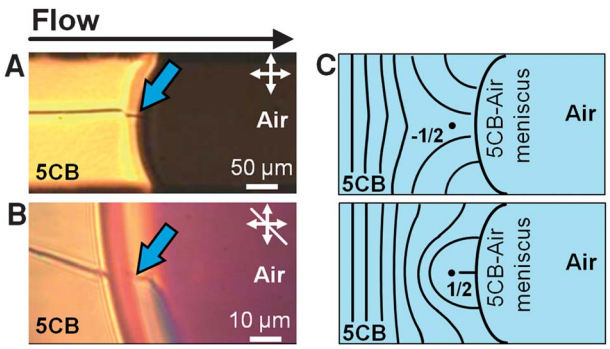

Fig. 4 Generation of disclination lines during filling the channel. (A) Polarizing micrograph (top view) showing the interface between nematic 5CB and air during the filling process. The blue pointer indicates the point of origin of the defect line at the meniscus. (B) By focusing using a high-magnification objective, the origin of the disclination was confirmed to be close to the glass surface. (C) Schematic of the director field (top view) close to the glass surface. At the 5CB–air interface, the molecules anchor perpendicularly, whereas in the upstream region, glass induces uniform planar anchoring. This leads to creation of the $\pm 1/2$ defect line, which is stabilized in the upstream portion due to the prevalent surface anchoring on the channel walls.

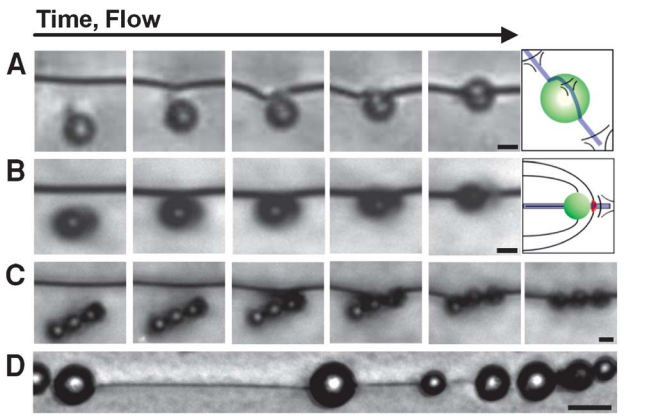

Fig. 5 Trap-and-transport processes. Time sequence of a colloidal particle docking to the soft rail: (A) Saturn-ring type, (B) dipolar type and (C) colloidal chain. The time increment between micrographs is 0.3 s; scale bar: 5 μm. (D) Droplet rail travelling on a disclination track; scale bar: 50 μm.

dipolar colloids were captured by the disclination (Fig. 5C), eventually leading to the desired 'trap-and-transport' phenomenon. Water droplets of sizes similar to the colloid particles exhibit analogous anisotropic colloidal interactions[31] when dispersed within the nematic host (perpendicular anchoring at the water–LC interface is easily achieved using a suitable surfactant[30]). As shown in Fig. 5D, a set of isolated droplets and a droplet chain were transported on the disclination line in an equivalent manner to the colloidal particles. Owing to the high monodispersity of the colloidal spheres, as compared to the droplets, we shall consider the former as our model cargo in the following sections.

To obtain quantitative information on the interaction between the particles and the disclination line, the motion of the particles was tracked as a function of time using digital video imaging. While, for a given particle size, the relative separation r between the particle and the disclination determined the long-range attractive interaction $F_{\text{disclination}}$, it was the average flow speed v which influenced the rate $\dot{r}$ at which the colloids approached the defect line. Fig. 6 plots the variation of the relative separation between a 5 μm particle and the disclination with time. This is depicted schematically in the top-right inset. The corresponding motion along the channel (x) and in the transverse direction (y) is plotted in the bottom-left inset. The local flow speed, $v = \dot{x} \approx 23$ μ s^{-1}, is evaluated from the slope of the $x(t)$ curve. Additionally, the linear behaviour of the particle trajectory along the y direction hints at a viscously damped motion, wherein the elasticity-mediated interaction $F_{\text{disclination}}$ is balanced by the Stokes drag force, F_{drag} (inset, top-right). The velocity of the approach of the particle towards the disclination line was evaluated directly from the derivative of the experimental data presented in Fig. 6. The net inertial force acting on the particle, obtained by balancing the attractive elastic force and the Stokes drag on the particle, thus reads:

$$m\ddot{r} = F_{\text{disclination}} - 6\pi a\eta_{\text{eff},y}\dot{r} \quad (2)$$

with m being the buoyant mass of the particle and $\eta_{\text{eff},y}$ the local effective viscosity experienced by the particle along the transverse direction.

The value of $\eta_{\text{eff},y}$ depends on the orientation of the director which in turn depends on the flow speed. The director orientation can be determined from the orientation of any colloidal particle bearing a dipolar defect which was observed to align along the local director. Similarly, for a cluster of dipolar particles, the local director orientation was determined from the alignment of the particle chain. The angular deviation relative to the initial orientation, ψ, is plotted in Fig. 7 as a function of flow speed. Below $v \approx 14$ μm s^{-1}, no significant deviation was observed. However, above a threshold speed, $v_c \approx 15.5$ μm s^{-1}, and critical Ericksen number, $Er \approx 10$ (for $w = 300$ μm, $d = 30$ μm, $\mu \approx 0.06$ Pa s), ψ increased in a non-linear fashion and approached $\psi \approx 77$ degrees at $v > 123$ μm s^{-1}. This behavior can be qualitatively explained as representing a Pieransky–Guyon instability[41,42] and reflects the usual bifurcation at the threshold speed. For $\psi < 60$ degrees $\psi = A(v - v_c)^{1/2}$, where $A \approx 9.6$ degrees(μm s^{-1})$^{-1/2}$ (Fig. 7, inset). Within the limits of finite width and anchoring on the channel walls, the value of Er at the threshold is in reasonable agreement with the predicted value, $Er_c = 12.84$.[41]

We can now obtain the effective viscosity of the medium in the transverse direction, $\eta_{\text{eff},y}$, using a combination of the Miesowicz viscosities and the director distortion ψ:[43]

$$\eta_{\text{eff},y} = (\eta_a - \eta_b)\sin\psi\cos\psi \quad (3)$$

where $\eta_a = 0.0326$ Pa s and $\eta_b = 0.0204$ Pa s are the Miesowicz viscosities for 5CB with the director being orthogonal to the velocity and its gradient and with the director being parallel to the velocity, respectively. For an isolated dipolar particle travelling at ≈30 μm s^{-1}, the effective viscosity $\eta_{\text{eff},y}$ is

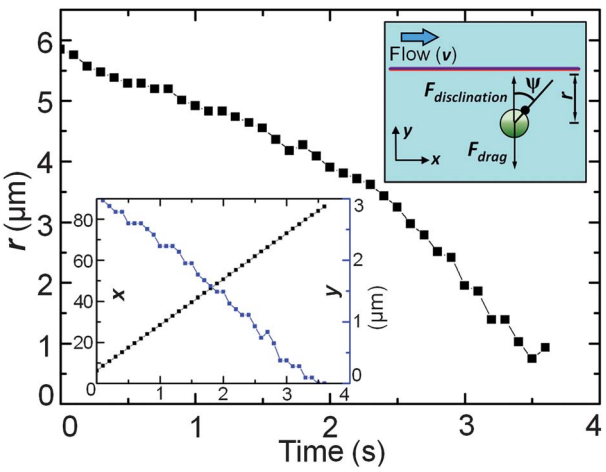

Fig. 6 Separation of a 5 μm dipolar colloid particle relative to the disclination as a function of time. Inset (bottom-left) shows the absolute distance along x (black dots) and y (blue dots) travelled by the particle over the same time. Inset (top-right) schematically represents the forces $F_{\text{disclination}}$ and F_{drag} acting (in addition to the flow drag) on the particle at a distance r from the disclination line. ψ denotes the flow-induced director distortion at a flow speed v.

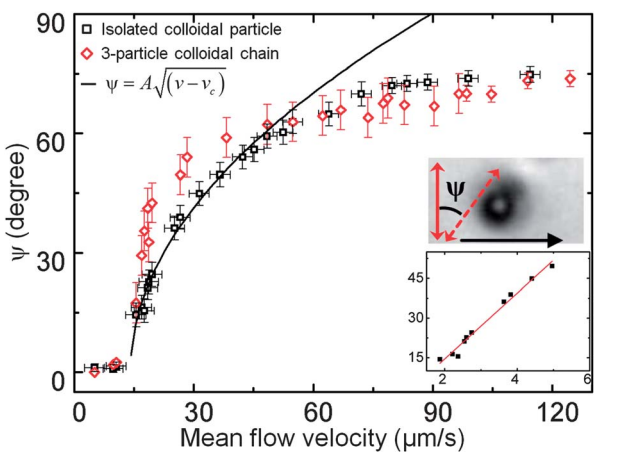

Fig. 7 Director-field mapping by colloids in flow. Angular deviation of dipolar defects and colloidal chains, relative to the static situation (see the polarized micrograph), plotted as a function of flow speed. The inset plot shows the linear dependence of ψ on $(v - v_c)^{1/2}$ (units are degrees on the y-axis and (μm s^{-1})$^{1/2}$ on the x-axis).

consequently ≈0.0061 Pa s. Since the inertial term in eqn (2) is significantly smaller than the Stokes drag, the particle transport in the transverse direction is indeed viscously damped, yielding:

$$F_{\text{disclination}} = 6\pi a\dot{r}\,(\eta_a - \eta_b)\,\sin\psi\cos\psi. \quad (4)$$

Fig. 8 plots the attractive force as a function of the relative separation. The corresponding flow speed (≈30 μm s^{-1}) distorts the initial director field by $\psi \approx 45$ degrees (see Fig. 7). The log–log plot (inset, top-right) shows a distinct power-law dependence of $F_{\text{disclination}} \sim r^{-n}$, yielding $n = 1.85 \pm 0.3$. This is in good agreement with the existing literature on the interaction between a dipolar colloid and a disclination line.[40] Furthermore, the scaling arguments require $F_{\text{disclination}}$ to be proportional to l^n, with l being the characteristic length scale—the particle radius a—of the system. Consequently, the attractive interaction at a given separation should scale up with the particle dimensions: larger the distortion within the ordered mesophase due to the particle, stronger is the interaction. Indeed this is observed qualitatively in our system: The attractive force on a two-particle chain is ≈35% higher than that on a single particle.

The rate $\dot{r}$, with which the particle approaches the disclination line, shows an additional non-linear dependence on the flow speed of the flowing matrix. Fig. 8 (inset, bottom-left) plots the variation of $\dot{r}$ as a function of the flow speed for a 5 μm particle. The rate of approach—influenced by the transverse viscosity coefficient—first decreased, followed by an increase. The effective viscosity in the transverse direction, which is coupled to the local director distortion, varies with the flow speed v. At low flow speeds, and correspondingly small director distortions, $\eta_{\text{eff},y} < \eta_{\text{eff},y}^{\max}$. Theoretically, the maximum transverse viscosity, $\eta_{\text{eff},y}^{\max}$, is attained at $\psi = 45$ degrees. Consequently, the particle experiences smaller drag forces, resulting in higher 'terminal' speeds. On the other hand, as the director distortion increases with v, $\eta_{\text{eff},y}$ reaches a maximum, beyond which $\eta_{\text{eff},y}$ again decreases. Correspondingly, as is reflected in Fig. 8 (inset, bottom-left), $\dot{r}$ first shows a dip, and then again increases.

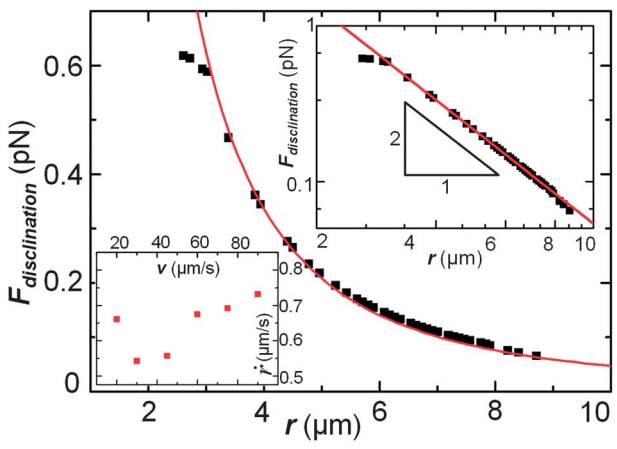

Fig. 8 Interaction between a disclination and a dipolar colloid in flow, plotted as a function of relative separation. Inset (top-right) presents the experimental data of the interaction on a log–log plot. The straight line indicates a power law dependence, with exponent $n \approx -2$. Inset (bottom-left) shows the variation of $\dot{r}$ as a function of v for a 5 μm particle.

The elasticity-mediated interactions between the colloidal particles and the disclination line are responsible for the trapping of the dispersed phases (colloids, droplets, *etc.*) on the soft rail. In comparison to the isotropic solvents, where colloidal interactions are determined by the attractive dispersion forces *vis-à-vis* repulsive steric or Coulombic forces, structural forces in LC systems are much stronger—typically on the order of a few pN (ref. 40 and 44)—and endow the transport system with high stability and thermodynamic robustness. Nevertheless, the particles/droplets anchored to the soft rail can be untrapped rather conveniently, for instance, by simply heating the system to the nematic–isotropic transition temperature (≈33 °C for 5CB). Above this temperature, the LC behaves as an isotropic fluid, devoid of any topological entity. Alternatively, the particles travelling along the defect line can be swerved out of the rail by introducing a curvature in the flow path. The micrograph sequence in Fig. 9A shows a particle escaping from the soft rail while traversing a curvature. The balance between viscous and elastic forces is essential for the stability of the particle on the disclination track. On encountering a curvature on the flow path (Fig. 9B and C), a component of the flow velocity tends to destabilize the particle motion. As depicted in Fig. 9C, the drag force corresponding to $v\cos\theta$ counteracts $F_{\text{disclination}}$. Viscous drag forces greater than $F_{\text{disclination}}$ can subsequently derail the colloidal particle. The stability criterion at the curvature thus reads:

$$F_{\text{disclination}} \geq 6\pi\eta_{\text{eff}} a v\cos\theta. \quad (5)$$

This effectively leaves us with a, v, and θ as experimental parameters to tune the stability of the particle on the soft rail. Interestingly, the equilibrium condition is a straightforward and alternative route to estimate the strength of the elastic force between the particle and the disclination line, $F_{\text{disclination}}$. For instance, relative to the viscous force on a 5 μm particle (see ESI Movie M3†), we estimated $F_{\text{disclination}} \approx 10$ pN, which is in fairly good agreement with the existing data.

4.3 Navigating the 'soft rail'

The position of the disclination line in the xy plane depends sensitively on the flow speed. Still, the range over which the disclination was shifted away from the channel wall towards the center has been rather small ($\Delta v \approx 10$ μm s^{-1} for a width of 200 μm), limiting its usefulness as a practical control parameter for positioning. The lateral position p of the disclination ($0 < p < w/2$) can be accurately controlled, however, by varying the relative angle φ ($0 < \varphi < 90$ degrees) between the initial director orientation, determined by the anchoring direction on the glass surface, and the primary flow direction. As plotted in Fig. 10A, the disclination occupied a central position ($w/2$) at high angles and was close to the channel wall at low angles ($\varphi \approx 20$ degrees). At even lower angles, the line was too close to the wall to be detected (Fig. 10A, inset). This anchoring-induced placement is crucial for controlling the position of the disclination

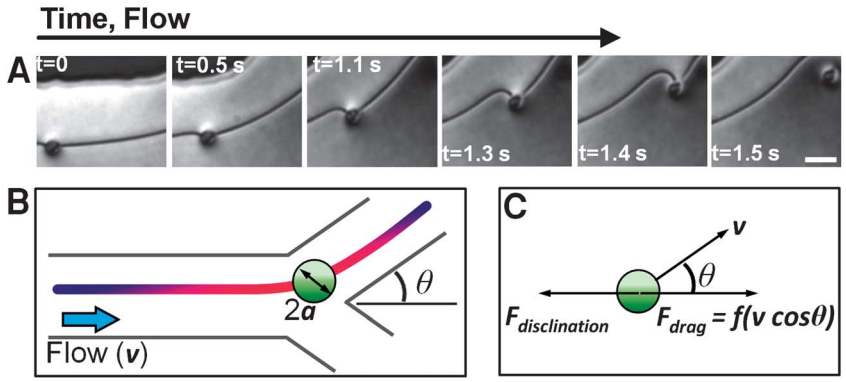

Fig. 9 Derailment of a colloid traversing a curve. (A) Micrograph time sequence showing a colloidal particle escaping from the soft rail. Scale bar: 20 μm. (B) The corresponding experimental parameters: flow speed, v, angle of the curvature, θ, and the particle radius, a. (C) Forces acting on the colloidal particle while traversing a curvature.

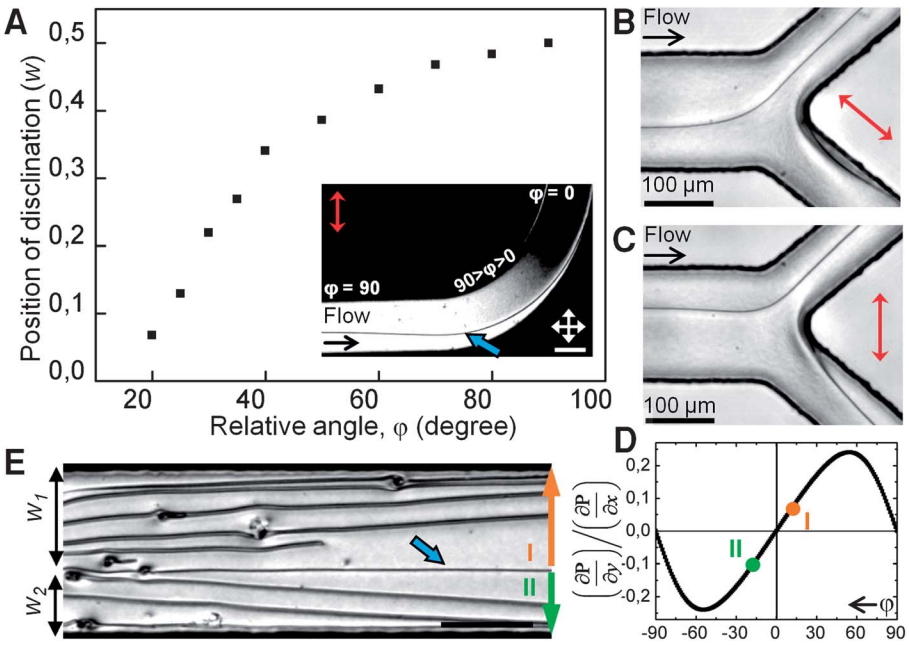

Fig. 10 Guiding the soft rail. (A) Plot representing the dependence of the disclination position on the relative angle φ between the flow direction and the initial director orientation, referenced to the channel center ($y = w/2$). The polarization micrograph in the inset shows the gradual shift of the defect line (marked by the blue arrow) as φ changes, anchoring is along the direction of the double-headed red arrow; scale bar: 100 μm. (B) The defect line was placed in the upper arm of a Y-junction by appropriate surface anchoring. (C) In a confinement with symmetric director configuration, the probability of the line to occupy either arm is equal. This arrangement can be used for switching the line between the arms. (D) Variation of the transverse pressure gradient with φ, calculated for 5CB and for each side of the defect line marked by the blue arrow in (E). The gradients corresponding to regions I (width w_1) and II (width w_2) are asymmetrical in this case (green and ochre points). Defects stretched from trapped impurities reflect the secondary flow, which is a result of the transverse pressure drop from the disclination to the channel walls; scale bar: 225 μm.

track and offers a fresh approach to guided transport in microfluidic devices, distinct from conventional railed or field-guided transports. As shown in Fig. 10B, the disclination can be placed specifically in the upper arm of the symmetrical Y-junction, where the relative angle φ is high compared with the lower arm ($\varphi_{upper} \gg \varphi_{lower}$). The colloidal cargo trapped by the defect line was therefore guided to this arm of the microchannel (see ESI Movie M4†). In contrast, transport through the rest of the nematic bulk was determined purely by the shape of the streamlines, which are symmetrically distributed relative to the junction. When $\varphi_{upper} \approx \varphi_{lower}$ (Fig. 10C), the line is similarly stable in either of the arms; over a large number of experiments, we observed occupation of either arm with equal likelihood. Moreover, due to the favorable anchoring shown in Fig. 10C, a second disclination developed in the lower arm, originating at the junction. Tailoring channel boundaries in this manner provides a route for *in situ* selection of a specified target. Switching of the defect line from one arm to the other was achieved through a simple flow manipulation (see ESI Movie M5†). Furthermore, it has been shown that surfaces can be designed in such a way that different anchoring states are stabilized, *e.g.*, by appropriate coating with grafted azo-benzene

compounds showing photo-induced isomerization,[45] or by means of micropatterned surfaces.[46]

The ability to navigate the disclination line is a result of the intricate coupling between the flow and the nematic director.[18] Close to the walls, the director adapts to the assigned boundary condition and reorients over a transition-boundary layer.[47] At higher speeds, the director undergoes flow-induced reorientation,[48] which in turn generates a secondary pressure gradient in the transverse direction, due to the anisotropic viscosity and flow-director coupling.[41,43] The disclination line divides the channel into two longitudinal sections characterized by opposite senses of director reorientation (Fig. 3F and ESI Fig. S3†). In each sector, there is a finite pressure drop from the center towards the channel walls. The symmetry is however broken when $\varphi \neq 90$ degrees and gradients occupy asymmetrical ordinates (Fig. 10D). The lateral position of the disclination line is then in essence determined by the balance of pressure P from either side

$$w_1\left(\frac{\partial P}{\partial y}\right)_1 = w_2\left(\frac{\partial P}{\partial y}\right)_2 \quad (6)$$

where $w_1 + w_2 = w$ (Fig. 10E). A visual confirmation of the resulting transverse flow[41,42] was obtained by observing defect lines stretched out from trapped impurities. They deviated from the primary flow direction (Fig. 10E), in contrast to our observations in systems that do not favor secondary flow (see ESI Fig. S4†).

5 Conclusion

We have demonstrated a novel approach to guided transport of a microfluidic cargo based on topological microfluidics. On the one hand, it serves as a ready-to-use, versatile platform for targeted delivery of a diverse set of dispersed phases (single particles, droplets, or clusters of such entities), on the other hand, it elucidates the forte of topological constraints in paving the way for flexible micro-cargo concepts. Our methods not only complement the existing techniques employed for guided transport, but also offer several competitive advantages, including the possibility of *in situ* switching between targets and minimal design challenges. In addition to the *in situ* switching demonstrated here, there are also established techniques at hand to switch between different states of anchoring at the walls and thereby to navigate the disclination lines by external control.[45,46] The LC-based microfluidic platform is well suited for a number of ancillary functions, *e.g.*, director field mapping by visualizing colloid orientations, and characterization of the interaction forces between topological entities. Based on the fundamental studies of topological interactions in microfluidic environments, the present work is envisaged to emerge as a novel dimension in the realm of micro-cargo transport, heralding the first steps of topological microfluidics.

Acknowledgements

The authors thank Jean-Christophe Baret, Paul Steffen, and Kristian Hantke for helpful discussions. The research was financially supported by the European Union (EC Marie Curie ITN project Hierarchy—PITN-CA-2008-215851).

References

1 D. R. Meldrum and M. R. Holl, *Science*, 2002, **297**, 1197.
2 J. Glückstad, *Nat. Mater.*, 2004, **3**, 9.
3 A. B. Subramaniam, M. Abkarian and H. A. Stone, *Nat. Mater.*, 2005, **4**, 553.
4 A. Terray, J. Oakey and D. W. M. Marl, *Science*, 2002, **296**, 1841.
5 R. Seemann, M. Brinkmann, T. Pfohl and S. Herminghaus, *Rep. Prog. Phys.*, 2011, **75**, 016601.
6 J. C. Baret, O. J. Miller, V. Taly, M. Ryckelynck, A. El-Harrak, L. Frenz, C. Rick, M. L. Samuels, J. B. Hutchison, J. J. Agresti, D. R. Link, D. A. Weitz and A. D. Griffiths, *Lab Chip*, 2009, **9**, 1850.
7 S. E. Chung, W. Park, S. Shin, S. A. Lee and S. Kwon, *Nat. Mater.*, 2008, **7**, 587.
8 P. Abbyad, R. Dangla, A. Alexandrou and C. N. Baroud, *Lab Chip*, 2011, **11**, 813.
9 M. Ravnik, G. P. Alexander, J. M. Yeomans and S. Žumer, *Proc. Natl. Acad. Sci. U. S. A.*, 2011, **108**, 5188.
10 T. Araki, M. Buscaglia, T. Bellini and H. Tanaka, *Nat. Mater.*, 2011, **10**, 303.
11 T. Ohzono and J. Fukuda, *Nat. Commun.*, 2012, **3**, 710.
12 Y.-K. Kim, B. Senyuk and O. D. Lavrentovich, *Nat. Commun.*, 2012, **3**, 1133.
13 A. Sengupta, S. Herminghaus and Ch. Bahr, *Mol. Cryst. Liq. Cryst.*, 2011, **547**, 203.
14 A. Sengupta, U. Tkalec and Ch. Bahr, *Soft Matter*, 2011, **7**, 6542.
15 M. Miesowicz, *Nature*, 1946, **158**, 27.
16 J. L. Ericksen, *Arch. Ration. Mech. Anal.*, 1959, **4**, 231.
17 F. M. Leslie, *Quart. J. Mech. Appl. Math.*, 1966, **19**, 357.
18 F. M. Leslie, *Arch. Ration. Mech. Anal.*, 1968, **28**, 265.
19 P. J. M. Vanbrabant, J. Beeckman, K. Neyts, R. James and F. A. Fernandez, *Appl. Phys. Lett.*, 2009, **95**, 151108.
20 G. Toth, C. Denniston and J. M. Yeomans, *Phys. Rev. Lett.*, 2002, **88**, 105504.
21 J. G. Cuennet, A. E. Vasdekis, L. De Sio and D. Psaltis, *Nat Photonics*, 2011, **5**, 234.
22 A. Sengupta, S. Herminghaus and Ch. Bahr, *Appl. Phys. Lett.*, 2012, **101**, 164101.
23 A. Sengupta, U. Tkalec, M. Ravnik, J. M. Yeomans, Ch. Bahr and S. Herminghaus, *Phys. Rev. Lett.*, 2013, **110**, 048303.
24 S. Chandrasekhar and G. S. Ranganath, *Adv. Phys.*, 1986, **35**, 507.
25 C. W. Oseen, *Trans. Faraday Soc.*, 1933, **29**, 883.
26 A. D. Price and D. K. Schwartz, *Langmuir*, 2006, **22**, 9753.
27 A. Sengupta, B. Schulz, E. Ouskova and Ch. Bahr, *Microfluid. Nanofluid.*, 2012, **13**, 941.
28 F. J. Kahn, *Appl. Phys. Lett.*, 1973, **22**, 386.
29 I. Muševič, M. Škarabot, U. Tkalec, M. Ravnik and S. Žumer, *Science*, 2006, **313**, 954.
30 J. M. Brake, A. D. Mezera and N. L. Abbott, *Langmuir*, 2003, **19**, 6436.

31 P. Poulin, H. Stark, T. C. Lubensky and D. A. Weitz, *Science*, 1997, **275**, 1770.
32 A. Sengupta, C. Pieper, J. Enderlein, Ch. Bahr and S. Herminghaus, *Soft Matter*, 2013, **9**, 1937.
33 P. Oswald and P. Pieranski, *Nematic and Cholesteric Liquid Crystals: Concepts and Physical Properties Illustrated by Experiments*, Taylor & Francis, Boca Raton, 2005, ch. B. III.
34 C. M. Dafermos, *Quart. J. Mech. Appl. Math.*, 1970, **23**, 549.
35 J. L. Ericksen, *Liquid Crystals and Ordered Fluids*, Plenum, New York, 1970.
36 P. E. Cladis, W. van Saarloos, P. L. Finn and A. R. Kortan, *Phys. Rev. Lett.*, 1987, **58**, 222.
37 G. Ryskin and M. Kremenetsky, *Phys. Rev. Lett.*, 1991, **67**, 1574.
38 H. Imura and K. Okano, *Phys. Lett. A*, 1973, **42**, 403.
39 J. Ignés-Mullol, J. Baudry and P. Oswald, *Phys. Rev. E: Stat., Nonlinear, Soft Matter Phys.*, 2001, **63**, 031701.
40 D. Pires, J.-B. Fleury and Y. Galerne, *Phys. Rev. Lett.*, 2007, **98**, 247801.
41 P. Manneville and E. Dubois-Violette, *J. Phys.*, 1976, **37**, 1115.
42 I. Jánossy, P. Pieranski and E. Guyon, *J. Phys.*, 1976, **37**, 1105.
43 P. Pieranski and E. Guyon, *Phys. Lett. A*, 1974, **49**, 237.
44 P. Poulin, V. Cabuil and D. A. Weitz, *Phys. Rev. Lett.*, 1997, **79**, 4862.
45 O. Yaroshchuk and Y. Reznikov, *J. Mater. Chem.*, 2012, **22**, 286.
46 J.-H. Kim, M. Yoneya and H. Yokoya, *Nature*, 2002, **420**, 159.
47 P. G. de Gennes and J. Prost, *The Physics of Liquid Crystals*, Oxford University Press, Oxford, 1993, p. 137.
48 P. Pieranski and E. Guyon, *Solid State Commun.*, 1973, **13**, 435.

